



**HAL**  
open science

## Multiscale modelling of polycrystalline UO<sub>2</sub>: full-field simulations (FFT) and model-reduction approach (NTFA)

Julien Labat, Rodrigue Largeton, Jean-Claude Michel, Bruno Michel

### ► To cite this version:

Julien Labat, Rodrigue Largeton, Jean-Claude Michel, Bruno Michel. Multiscale modelling of polycrystalline UO<sub>2</sub>: full-field simulations (FFT) and model-reduction approach (NTFA). 25ème Congrès Français de Mécanique, Aug 2022, Nantes, France. 12 p. hal-03797442

**HAL Id: hal-03797442**

**<https://hal.science/hal-03797442>**

Submitted on 4 Oct 2022

**HAL** is a multi-disciplinary open access archive for the deposit and dissemination of scientific research documents, whether they are published or not. The documents may come from teaching and research institutions in France or abroad, or from public or private research centers.

L'archive ouverte pluridisciplinaire **HAL**, est destinée au dépôt et à la diffusion de documents scientifiques de niveau recherche, publiés ou non, émanant des établissements d'enseignement et de recherche français ou étrangers, des laboratoires publics ou privés.

# Multiscale modelling of polycrystalline $UO_2$ : full-field simulations (FFT) and model-reduction approach (NTFA)

J. LABAT<sup>a,b</sup>, R. LARGENTON<sup>a</sup>, J.-C. MICHEL<sup>b</sup>, B. MICHEL<sup>c</sup>

a. EDF-R&D, MMC, F-77818 Moret-sur-Loing Cedex, France

julien.labat@edf.fr, rodrigue.largenton@edf.fr

b. Aix Marseille Univ, CNRS, Centrale Marseille, LMA UMR 7031, Marseille, France

michel@lma.cnrs-mrs.fr

c. CEA, DES/IRESNE/DEC/SESC/LSC, Saint-Paul-lez-Durance, 13108, France

bruno.michel@cea.fr

## Résumé :

*Cette étude présente une modélisation micromécanique du comportement du dioxyde d'uranium ( $UO_2$ ), céramique polycristalline utilisée dans les réacteurs à eau pressurisée, par une approche en champs complets [17] et un modèle d'ordre réduit NTFA-TSO [15], pour des sollicitations typiques d'un accident d'insertion de réactivité. Au-delà d'une certaine température, l' $UO_2$  a un comportement élasto-viscoplastique avec un écrouissage dépendant des conditions de sollicitations en température et vitesse de déformation ( $T, \dot{\varepsilon}$ ). Dans un premier temps et via l'approche en champs complets, une calibration inverse de la loi d'évolution locale (loi monocristalline élasto-viscoplastique avec écrouissage) est réalisée à partir des données expérimentales obtenues à l'échelle macroscopique [13, 16]. Dans un deuxième temps, le modèle NTFA-TSO [15] est développé et appliqué au problème en question en utilisant deux approches : l'écrouissage pris constant par grain comme dans la référence [15], ou décomposé à l'image des modes associés à la déformation viscoplastique. Enfin et pour trois cas de chargements étudiés, les deux approches sont comparées. Les réponses macroscopiques de ces deux approches (FFT et NTFA-TSO) sont également comparées aux réponses expérimentales [13, 16].*

## Abstract:

*This numerical study presents a micromechanical modelling of uranium dioxide, a polycrystalline ceramic used in pressurised water reactors, using a full-field (FFT [17]) approach and a reduced order (NTFA-TSO [15]) model for loading conditions representative of a reactivity initiated accident. Above a transition temperature,  $UO_2$  exhibits an elasto-viscoplastic behaviour with strain hardening sensitive to the loading conditions temperature and macroscopic strain rate ( $T, \dot{\varepsilon}$ ). In a first step and via the Full-Field approach, an inverse calibration of the local viscoplastic strain-hardening evolution law is performed based on macroscopic scale experimental data [13, 16]. In a second step, the NTFA-TSO model [15] is developed and applied to the problem by using two approaches: the strain hardening taken, as in the reference [15], as constant per grain or taken as decomposed, like modes associated with viscoplastic deformation. Finally and for three cases, the two approaches are compared macroscopically and locally. The macroscopic responses of these two approaches are also compared to experimental results [13, 16].*

**Keywords:** polycrystal, model reduction, elasto-viscoplasticity

# 1 Introduction

Uranium dioxide ( $\text{UO}_2$ ) is a polycrystalline ceramic used as nuclear fuel within Pressurised Water Reactors (PWR). To account for the behaviour of this material during a Reactivity Initiated Accident (RIA), characterised by macroscopic strain rates  $\dot{\varepsilon} \in [0.1, 10.] [s]^{-1}$  and temperatures  $T \in [500, 2400] [^\circ C]$ , a micro-mechanical approach is adopted. In this study,  $\text{UO}_2$  is studied above a temperature ( $T > 1000 [^\circ C]$ ), which the material exhibits an elasto-viscoplastic behaviour with strain hardening. Assumption is made at the single crystal scale that the viscoplastic strain is entirely induced by the sliding of dislocation lines overcoming the Peierls barrier energy [1]. An empirical thermally activated plasticity law [10] is adopted to model this behaviour with consideration of the strain hardening. An inverse calibration, based on observations made at the single crystal scale [4, 5, 6], is performed (cf. part two) in the aim to determine the numerical values of the parameters composing the evolutions laws. This inverse calibration take into account the sensitivities to the loading parameters ( $T, \dot{\varepsilon}$ ). Once validated at the polycrystalline scale on uniaxial compressive strain tests [13, 16], the full-field FFT [17] numerical simulations are taken as reference to develop (cf. part three) and validate (cf. part four) a reduced-order model.

This model being used in the future within an industrial code of the fuel rod behaviour, it appeared necessary to use a reduced-order model to obtain reasonable computational costs. The Non-uniform Transformation Field Analysis Tangent Second Order (NTFA-TSO [15]) is used and developed for our study case (cf. part three). The agreements between NTFA-TSO model and full-field simulations (FFT) are checked on the macroscopic responses and local fields on three uniaxial loadings (cf. part four). It is checked that the numerical results of NTFA-TSO model are not deteriorated either macroscopically or locally by using two approaches: strain hardening taken as constant per grain, as in the reference [15], or decomposed, like the viscoplastic strain, on modes.

## 2 Mechanical problem and inverse calibration

### 2.1 Constitutive relations and local problem

The constitutive relations are based on the expression of the free-energy defined as:

$$w(\varepsilon, \varepsilon_{vp}, p) = \frac{1}{2} (\varepsilon - \varepsilon_{vp}) : \mathbf{L} : (\varepsilon - \varepsilon_{vp}) + w^{\text{iso}}(p), \quad \boldsymbol{\sigma} = \frac{\partial w}{\partial \varepsilon}(\varepsilon, \varepsilon_{vp}, p), \quad (1)$$

by which the expression of the stress tensor  $\boldsymbol{\sigma}$  is derived. This expression, which respects the generalized standard material structure, involves two internal variables, the viscoplastic strain  $\varepsilon_{vp}$  associated with its thermodynamic force  $\mathcal{A}_{vp} (\equiv \boldsymbol{\sigma})$  and the strain hardening variable  $p = (p_i), i \in \{\{100\}, \{110\}\}$  referring to a slip family of the studied material, associated with its thermodynamic force  $\mathcal{A}_p = (\mathcal{A}_{p,i})$ . The total strain  $\varepsilon$  is expressed as:

$$\varepsilon(\mathbf{x}, t) = \varepsilon_e(\mathbf{x}, t) + \varepsilon_{vp}(\mathbf{x}, t), \quad \varepsilon_{vp}(\mathbf{x}, t) = \sum_s \gamma_s^{\text{vp}}(\mathbf{x}, t) \mathbf{m}_s(\mathbf{x}), \quad (2)$$

with  $\varepsilon_e$  the elastic strain tensor and  $\varepsilon_{vp}$  the viscoplastic strain tensor. The latter tensor is a combination of the Schmid tensors ( $\mathbf{m}_s$ ) weighted by the slip ( $\gamma_s^{\text{vp}}$ ) on the considered system ( $s$ ). The slip systems are specific to the fluorite crystallographic structure of uranium dioxide [12].

The local problem is based on the existence of two dissipation potentials  $\psi_{vp}$  and  $\psi_p$  dependant on the two thermodynamics forces. The expressions [10] of these two potentials allow to establish the evolution laws of the different internal variables ( $\dot{\epsilon}_{vp}$  and  $\dot{p}_i$ ).

$$\begin{aligned}\psi_{vp} &= \sum_s \psi_{vp,s}, \quad \psi_{vp,s}(\mathcal{A}_{vp}, \mathcal{A}_{p,i}) = \dot{\gamma}_i^0 \times \frac{-\mathcal{A}_{p,i}}{n_i + 1} \times \left( \frac{|\mathcal{A}_{vp,s}|}{-\mathcal{A}_{p,i}} \right)^{n_i+1}, \\ \psi_p &= \sum_s \psi_{p,s}, \quad \psi_{p,s}(\mathcal{A}_{vp}, \mathcal{A}_{p,i}) = \dot{\gamma}_i^0 \times \frac{|\mathcal{A}_{vp,s}|}{(n_i - 1)} \times \left( \frac{|\mathcal{A}_{vp,s}|}{-\mathcal{A}_{p,i}} \right)^{n_i-1},\end{aligned}\quad (3)$$

where  $\mathcal{A}_{vp,s}(\mathbf{x}, t) = \mathcal{A}_{vp}(\mathbf{x}, t) : \mathbf{m}_s(\mathbf{x}) (\equiv \boldsymbol{\sigma}(\mathbf{x}, t) : \mathbf{m}_s(\mathbf{x}))$  is the projection of the thermodynamic force onto the Schmid tensor and  $\mathcal{A}_p = \mathcal{A}_{p,i}$  if  $s \in S_i$  with  $S_i$  all the sliding systems included in the family  $i$  ( $i \in \{\{100\}, \{110\}\}$ ). There are 3 families as used in [18]. However, the last family  $\{111\}$  is omitted due to the lack of experimental data [4, 6]. For our case, the expression of  $\mathcal{A}_{p,i}$  is given by:

$$\begin{aligned}\mathcal{A}_{p,i}(\mathbf{x}, t) &= -r_i(\mathbf{x}, t), \quad r_i(\mathbf{x}, t) = \tau_i^0(T, \dot{\epsilon}) + h_i(T, \dot{\epsilon}) \times p_i(\mathbf{x}, t), \\ \dot{p}_i &= \sum_{s \in S_i} \dot{\gamma}_s^p(\mathcal{A}_{vp}, \mathcal{A}_p), \quad \dot{\gamma}_s^p = |\dot{\gamma}_s^{vp}|.\end{aligned}\quad (4)$$

The local problem to be solved on the RVE  $V$  is summarised by the system of equations (5) coupled with the evolution laws of the internal variables (6) i.e. the viscoplastic strain and the strain hardening. It remains to determine the parameters of these evolution laws within part 2.2: parameters  $\tau_i^0(T, \dot{\epsilon})$ ,  $h_i(T, \dot{\epsilon})$  which are sensitive to the loading condition in particular the temperature and the macroscopic strain rate.

$$\left. \begin{aligned}\boldsymbol{\sigma}(\mathbf{x}, t) &= \mathbf{L}(\mathbf{x}) : (\boldsymbol{\epsilon}(\mathbf{x}, t) - \boldsymbol{\epsilon}_{vp}(\mathbf{x}, t)), \\ \text{div } \boldsymbol{\sigma}(\mathbf{x}, t) &= 0, \quad \boldsymbol{\sigma}(\mathbf{x}, t) \cdot \mathbf{n}(\mathbf{x}) \text{ antiperiodic on } \partial V, \\ \boldsymbol{\epsilon}(\mathbf{x}, t) &= \bar{\boldsymbol{\epsilon}}(t) + \frac{1}{2}(\nabla \mathbf{u}^*(\mathbf{x}, t) + \nabla \mathbf{u}^{*T}(\mathbf{x}, t)), \quad \mathbf{u}^*(\mathbf{x}, t) \text{ periodic on } \partial V.\end{aligned}\right\} \quad (5)$$

$$\dot{\gamma}_s^{vp} = \frac{\partial \psi_{vp,s}}{\partial \mathcal{A}_{vp,s}}(\mathcal{A}_{vp,s}, \mathcal{A}_{p,i}), \quad \dot{\gamma}_s^p = \frac{\partial \psi_{p,s}}{\partial \mathcal{A}_{p,i}}(\mathcal{A}_{vp,s}, \mathcal{A}_{p,i}), \quad s \in S_i. \quad (6)$$

## 2.2 Inverse calibration

In this study, the FFT method is used to solve the problem (5) coupled with evolution equations (6) on a polycrystalline representative volume element  $V$  (**Figure 1:(b)**) composed of 500 grains and discretised by  $135^3$  voxels. The assumption of small perturbations is adopted. The experimental measurements of [13, 16] are used.

This inverse calibration process, which aims to recover the asymptotic behaviour, is illustrated in **Figure 1:(a)**. It consists of two steps. In the first step, the work hardening part is omitted ( $h_i(T, \dot{\epsilon}) = 0$ ). The crossing stress  $\bar{\sigma}_{33}^{cr}$ , which is defined as the stress corresponding to the strain for which the straight line resulting from the elasticity behaviour crosses the straight line resulting from the asymptotic strain hardening behaviour, is calibrated using the expression of  $\tau_i^0(T, \dot{\epsilon})$ . The second step, based on the previously obtained expression of  $\tau_i^0(T, \dot{\epsilon})$ , focuses on the strain-hardening part and in particular on the expression of  $h_i(T, \dot{\epsilon})$ . The  $\dot{\gamma}_i^0(\dot{\epsilon})$  term is determined using numerical uni axial strain test at given strain rate at the single crystal scale and for an orientation that mobilises only one of the two slip families considered. The term  $\dot{\gamma}_i^0(\dot{\epsilon})$  is taken equal to the strain rate obtained on the sliding system. Finally, the

exponent  $n_i$  is fixed and deduced from the observations made at the polycrystalline scale [13, 16]:

$$n_{\{100\}} = 4, \dot{\gamma}_{\{100\}}^0(\dot{\varepsilon}) = 0.7 \times \dot{\varepsilon} \text{ and } n_{\{110\}} = 4, \dot{\gamma}_{\{110\}}^0(\dot{\varepsilon}) = 0.5 \times \dot{\varepsilon}, \quad (7)$$

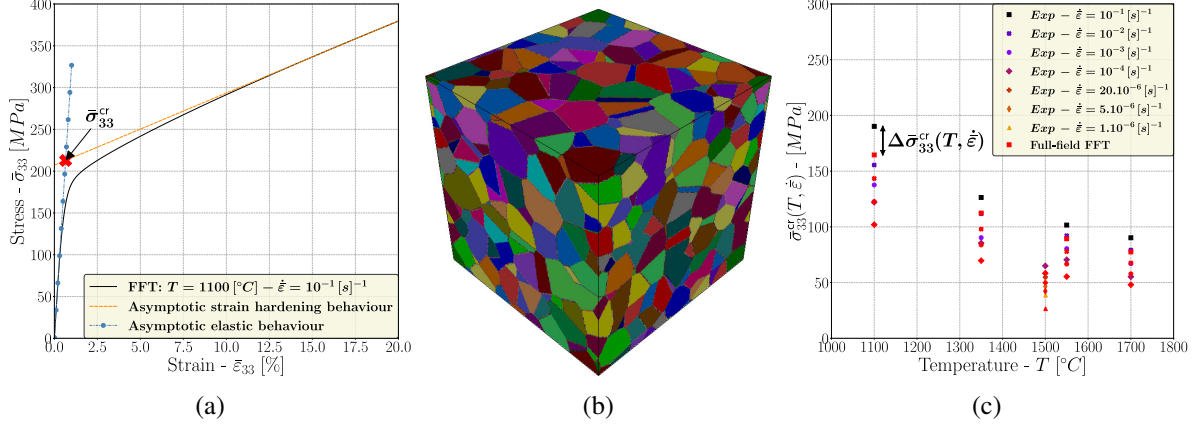


Figure 1: **(a):** Definition of the macroscopic cross stress  $\bar{\sigma}_{33}^{cr}$  for a given example. **(b):** Representative Volume Element (RVE) with 500 grains and  $135^3$  voxels on which the mechanical problem (5-6) is solved with FFT method. **(c):** Deviation of the macroscopic cross stress  $\Delta \bar{\sigma}_{33}^{cr}(T, \dot{\varepsilon})$  between the numerical values (Full-field FFT [17]) for a given iteration and the experimental data (Exp - [13, 16]).

### 2.2.1 Calibration of $\tau_i^0(T, \dot{\varepsilon})$

The initiation of the iterative process is based on observations made on experiments at the single crystal scale [4, 5, 6]. It is noted that the viscoplasticity yield stress of the  $\{100\}$  family is lower than the one of the second family retained, i.e. the  $\{110\}$  family. The ratio is about 2-3 between these two families and seems to decrease as the temperature increases. It is also noticed that the viscoplastic yield stress decreases when the temperature increases or when the strain rate decreases. The expression of  $\tau_i^0(T, \dot{\varepsilon})$ , based on the above observations is taken as:

$$\tau_i^0(T, \dot{\varepsilon}) = A_i^f(\dot{\varepsilon}) \times \exp(-b_i^f \times T) + C_i^f(\dot{\varepsilon}), \quad (8)$$

$$A_i^f(\dot{\varepsilon}) = \text{Max} \left[ a_i^{f,0} - a_i^{f,1} \times \exp[-a_i^{f,2} \times \log_{10}(\dot{\varepsilon})], 0 \right],$$

with  $C_i^f(\dot{\varepsilon})$  having the same strain rate dependence as  $A_i^f(\dot{\varepsilon})$  with the flowing parameters:  $c_i^{f,0}$ ,  $c_i^{f,1}$ ,  $c_i^{f,2}$ . The iterative process focuses on determining the set of parameters constituting  $A_i^f$ ,  $b_i^f$ ,  $C_i^f$  by minimising the error using a least squares method, the Levenberg Marquardt method [2, 3]. The minimisation is performed on  $\tau_i^0(T, \dot{\varepsilon})$  with respect to the available experimental crossing stress obtained at the macroscopic scale and transposed to the local scale. The critical issue is to transpose the macroscopic [13, 16] data into local data in order to provide the numerical data necessary to perform a least square minimisation and express the parameters of  $\tau_i^0(T, \dot{\varepsilon})$ .

By noting ( $n$ ) the number of the iteration, the iterative process is defined as:

$$\tau_i^{0,(n+1)}(T, \dot{\varepsilon}) = \tau_i^{0,(n)}(T, \dot{\varepsilon}) + f_s \times {}^{(n)}\Delta \bar{\sigma}_{33}^{cr}(T, \dot{\varepsilon}), \quad (9)$$

where  $f_s$  is the Schmid factor of the ( $s$ ) system ( $f_s = \Sigma_0 : m_s(x)$ ,  $\Sigma_0$  the direction of applied stress).

${}^{(n)}\Delta\bar{\sigma}_{33}^{cr}(T, \dot{\varepsilon})$  is the error, at the given loading conditions (see **Figure 1:(c)**), between the experimental crossing stress and the crossing stress resulting from the FFT simulation carried out on RVE **Figure 1:(b)** with the determined parameters of  $\tau_i^0(T, \dot{\varepsilon})$  at iteration  $(n)$  ( $\tau_i^{0,(n)}(T, \dot{\varepsilon})$ ). Finally, the data set necessary to use a least squares method in order to obtain the numerical values of the parameters at iteration  $(n+1)$  is deduced from (9):  $\tau_i^{0,(n+1)}(T, \dot{\varepsilon})$ . Then parameters of  $\tau_i^0(T, \dot{\varepsilon})$  at iteration  $(n+1)$  are obtained. The relative error at iteration  $(n)$ ,  $Er^{(n)}$ , is calculated and a relative stopping criterion  $\delta$ ,  $\delta = 10^{-3}$  is used with:

$$Er^{(n)} = \frac{1}{N} \times \sum |{}^{(n)}\Delta\bar{\sigma}_{33}^{cr}(T, \dot{\varepsilon})|, |Er^{(n)} - Er^{(n-1)}| < \delta \times Er^{(n-1)}, \quad (10)$$

where  $N$  is the number of experimental measurements used.

## 2.2.2 Calibration of $h(T, \dot{\varepsilon})$

The strain hardening is defined by family and is a function of the cumulated viscoplastic strain on all the sliding systems composing the family. Due to lack of experimental data, the coefficient  $h_i$  of strain hardening is taken equal for both families, i.e.:  $h_{\{100\}} = h_{\{110\}} = h$ . In a first step, the asymptotic strain hardening slope of the selected macroscopic experimental curves [13, 16] is determined. For the same loading conditions, the value of  $h$  that numerically generates the same slope is calculated by successive iterations using the following iterative process:

$$h^{(n+1)} = \frac{a_{p,exp} \times h^{(n)}}{a_{p,simu}^{(n)}}, |a_{p,simu}^{(n)} - a_{p,simu}^{(n-1)}| < \delta \times a_{p,exp}, \quad (11)$$

with  $a_{p,exp}$  the experimental strain hardening slope and  $a_{p,simu}^{(n)}$  the numerical strain hardening slope. The stopping criterion is similar to the one previously used, with  $\delta = 10^{-4}$ .

Once the set of numerical values has been obtained, a function that has the correct asymptotic behaviour deduced from the observations [13, 16] is specified. The slope decreases and tends to zero as the temperature increases. The slope decreases until it reaches a threshold when the strain rate decreases. The expression of  $h(T, \dot{\varepsilon})$  is given as:

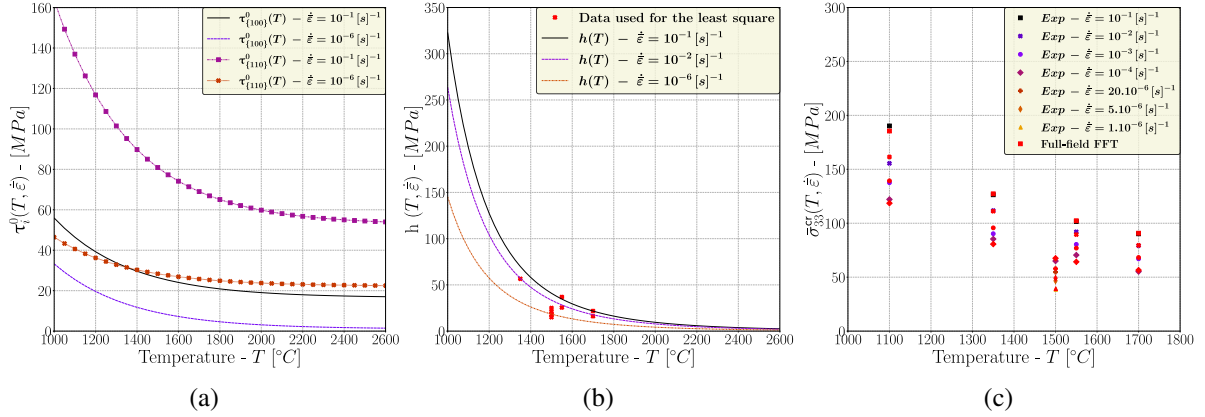
$$h(T, \dot{\varepsilon}) = \frac{a^h \times \ln(b^h \times \dot{\varepsilon} + f^h)}{(c^h \times T + d^h)^{e^h}}. \quad (12)$$

Again, when the stopping criterion is satisfied, a least squares method is used to deduce the parameters of  $h$  minimising the distance to the selected data ( $h^{(n+1)}(T, \dot{\varepsilon})$ ).

## 2.2.3 Results of the inverse calibration

The numerical values of the parameters intervening in the expression of  $\tau_i^0(T, \dot{\varepsilon})$  and  $h(T, \dot{\varepsilon})$  and resulting from the iterative processes are compiled in **Tab 1**. The variation of the  $\tau_i^0(T, \dot{\varepsilon})$  and  $h(T, \dot{\varepsilon})$ , for the numerical values presented in **Tab 1**, are illustrated in **Figure 2:(a,b)** for some loading conditions. The comparison of crossing stresses on the set of experimental data used, at the end of the iterative processes, is shown in **Figure 2:(c)**.

Numerical data	$A_i^f$	$(a, c)_i^{f,0} [MPa], (a, c)_i^{f,k} [-], k \in \{1, 2\} [-]$	$b_i^f [^\circ C]^{-1}$
	$C_i^f$		
{100}	$a^{f,0} = 1.5626 \times 10^6$	$\  a^{f,1} = 1.5619 \times 10^6 \  a^{f,2} = 1.6853 \times 10^{-5}$	$b^f = 2.8 \times 10^{-3}$
	$c^{f,0} = 2.0793 \times 10^1$	$\  c^{f,1} = 3.1253 \times 10^0 \  c^{f,2} = 3.0463 \times 10^{-1}$	
{110}	$a^{f,0} = 0$	$\  a^{f,1} = -2.2 \times 10^3 \  a^{f,2} = -2.9 \times 10^{-1}$	$b^f = 2.7 \times 10^{-3}$
	$c^{f,0} = 0$	$\  c^{f,1} = -6.2 \times 10^1 \  c^{f,2} = -1.8 \times 10^{-1}$	
h	$a^h = 9.1 \times 10^4 [MPa]$	$\  b^h = 2.8 \times 10^4 [s]^{-1} \  c^h = 5.2 \times 10^{-3} [^\circ C]^{-1}$	
	$d^h = -1.2 \times 10^{-1} [-]$	$\  e^h = 5. \times 10^0 [-] \  f^h = 2.8 \times 10^2 [-]$	

Table 1: Numerical values of parameters involved in the expression of  $\tau_i^0(T, \dot{\varepsilon})$  and  $h(T, \dot{\varepsilon})$ .Figure 2: **(a,b):**  $\tau_i^0(T, \dot{\varepsilon})$  and  $h(T, \dot{\varepsilon})$  as functions of temperature and macroscopic strain rate for given macroscopic strain rate. **(c):** Comparison of the macroscopic crossing stress  $\bar{\sigma}_{33}^{Cr}$ : numerical values (Full-Field FFT) in red symbols and experimental data (Exp - [13, 16]) in color symbols.

The full-field model is considered to be sufficiently accurate with respect to the experimental results. It is possible to develop a reduced-order model in order to integrate it into an industrial computational code. To this end, the NTFA-TSO model [15] is chosen and developed for our study case in the following section.

### 3 NTFA-TSO

#### 3.1 Decomposition of the internal variable

The basic feature of the NTFA theory [8] is a decomposition of the fields of internal variables, namely here the viscoplastic strain and the strain hardening variables, into a linear combinations of predetermined shape functions (called modes), having the same tensor character as the considered variables. The modes ( $\mu_{vp}, \mu_{p,i}$ ) are constant with respect to time but support the heterogeneity of the RVE. They are weighted by the reduced internal variables ( $\xi_{vp}, \xi_{p,i}$ ):

$$\varepsilon_{vp}(\mathbf{x}, t) = \sum_k^{M_{vp}} \xi_{vp}^{(k)}(t) \mu_{vp}^{(k)}(\mathbf{x}), p_i(\mathbf{x}, t) = \begin{cases} \sum_l^{M_{p,i}} \xi_{p,i}^{(l)}(t) \mu_{p,i}^{(l)}(\mathbf{x}) - [\mathbf{Dec}], \\ \sum_g \xi_{p,i}^{(g)}(t) \chi^{(g)}(\mathbf{x}) - [\mathbf{Cpg}]. \end{cases} \quad (13)$$

The decomposition of the viscoplastic strain tensor is taken from the reference [15]. Classically this tensor is decomposed on a finite number  $M_{vp}$  of modes. As for the strain hardening variable, two decompositions are considered. The first one is taken from the reference [15] and consists in considering

the strain hardening constant per grain ( $g$ ) [Cpg]. The second, inspired by the literature, consists in decomposing this variable on a finite number  $M_{p,i}$  of modes [Dec].

### 3.2 Macroscopic state law and influence tensors

With the NTFA decomposition (13), the macroscopic state variables of the effective constitutive relations are the macroscopic strain ( $\bar{\varepsilon}$ ) and the reduced internal variables ( $\xi_{vp}$ ,  $\xi_{p,i}$ ). The local strain field  $\varepsilon(\mathbf{x}, t)$  solution of the linear thermoelastic problem (5) with decompositions (13) can be expressed by superposition as:

$$\varepsilon(\mathbf{x}, t) = \mathbf{A}(\mathbf{x}) : \bar{\varepsilon}(t) + \sum_l^{M_{vp}} \mathbf{D} * \mu_{vp}^{(l)}(\mathbf{x}) \xi_{vp}^{(l)}(t), \quad (14)$$

with  $\mathbf{A}(\mathbf{x})$  the elastic strain localization tensor,  $\mathbf{D} * \mu_{vp}^{(l)}(\mathbf{x}) = \frac{1}{|V|} \int_V \mathbf{D}(\mathbf{x}, \mathbf{x}') : \mu_{vp}^{(l)}(\mathbf{x}') d\mathbf{x}'$  and

$\mathbf{D}(\mathbf{x}, \mathbf{x}') = \mathbf{\Gamma}(\mathbf{x}, \mathbf{x}') : \mathbf{L}(\mathbf{x}')$  where  $\mathbf{D}$  is the nonlocal operator and  $\mathbf{\Gamma}$  is the nonlocal Green operator.

The decomposition made on the viscoplastic strain tensor ensures the separation of the spatial variable ( $\mathbf{x}$ ) from the temporal variable ( $t$ ). Therefore, the calculation of  $\mathbf{D} * \varepsilon_{vp}(\mathbf{x}, t)$  has to be done only once and for all by calculating for all the modes retained  $\mathbf{D} * \mu_{vp}^{(l)}(\mathbf{x})$ . The elastic strain localization tensor  $\mathbf{A}(\mathbf{x})$  and the influence tensors  $\mathbf{D} * \mu_{vp}^{(l)}(\mathbf{x})$  can be computed once and for all by solving  $6 + M_{vp}$  linear elasticity problems (see [11]). The stress tensor is then expressed as:

$$\begin{aligned} \boldsymbol{\sigma}(\mathbf{x}, t) &= \mathbf{L}(\mathbf{x}) : \mathbf{A}(\mathbf{x}) : \bar{\varepsilon}(t) + \sum_l^{M_{vp}} \boldsymbol{\rho}_{vp}^{(l)}(\mathbf{x}) \xi_{vp}^{(l)}(t), \\ \boldsymbol{\rho}_{vp}^{(k)}(\mathbf{x}) &= \mathbf{L}(\mathbf{x}) : \left( \left( \mathbf{D} * \mu_{vp}^{(k)} \right) (\mathbf{x}) - \mu_{vp}^{(k)}(\mathbf{x}) \right), \end{aligned} \quad (15)$$

Knowing that the effective free energy  $\bar{w}$  is the average over the RVE of the local free energy  $w$ , the thermodynamic forces associated with the macroscopic state variables read:

$$\begin{aligned} \frac{\partial \bar{w}}{\partial \bar{\varepsilon}} &= \bar{\boldsymbol{\sigma}}, \quad \bar{\boldsymbol{\sigma}} = \tilde{\mathbf{L}} : \bar{\varepsilon} + \sum_k^{M_{vp}} \langle \boldsymbol{\rho}_{vp}^{(k)} \rangle \xi_{vp}^{(l)}, \\ -\frac{\partial \bar{w}}{\partial \xi_{vp}^{(k)}} &= a_{vp}^{(k)}, \quad a_{vp}^{(k)} = \bar{\varepsilon} : \mathbf{a}^{(k)} + \sum_l \langle \mu_{vp}^{(k)} : \boldsymbol{\rho}_{vp}^{(l)} \rangle \xi_{vp}^{(l)}, \\ -\frac{\partial \bar{w}}{\partial \xi_{p,i}^{(k)}} &= a_{p,i}^{(k)}, \quad a_{p,i}^{(k)} = \left[ \begin{array}{l} - \left( \tau_i^0 \langle \mu_{p_i}^{(k)} \rangle + h_i \times \sum_l^{M_{p,i}} \xi_{p_i}^{(l)} \langle \mu_{p_i}^{(k)} \mu_{p_i}^{(l)} \rangle \right) - [\mathbf{Dec}], \\ - \left( \tau_i^0 + h_i \times \xi_{p_i}^{(k)} \right) \times c^{(k)} - [\mathbf{Cpg}], \end{array} \right] \end{aligned} \quad (16)$$

with  $\mathbf{a}^{(k)} = \langle \mu_{vp}^{(k)} : \mathbf{L} : \mathbf{A} \rangle$  and where  $\tilde{\mathbf{L}} = \langle \mathbf{L} : \mathbf{A} \rangle$  is the effective elastic stiffness tensor.

### 3.3 Complementary evolution laws by tangent second-order linearisation of the effective dissipation potential

It remains to specify the evolution laws of the new homogenized internal variables ( $\dot{\xi}_{vp}$ ,  $\dot{\xi}_{p,i}$ ) or by duality, the evolution laws of the thermodynamics forces ( $\dot{a}_{vp}$ ,  $\dot{a}_{p,i}$ ) associated to these new variables.

Fritzen and Leuschner [9] have proposed an hybrid formulation making use of the effective dissipation potential, defined by:

$$\psi^{\text{hom}} = \tilde{\psi}, \tilde{\psi} = \langle \psi \rangle, \langle \psi \rangle = \sum_g c^{(g)} \sum_s \langle \psi_s \rangle^{(g)}, \quad (17)$$

with  $c^{(g)}$  the volume fraction. It has been shown [14] that this formulation of the effective dissipation potential is not exact in its definition but can be a good approximation when enough modes are taken in the decomposition (13). Based on this approximation of the effective dissipation potential, the evolution laws of the new thermodynamic forces are given by:

$$\begin{aligned} \dot{a}_{\text{vp}}^{(k)}(\bar{\varepsilon}, \xi_{\text{vp}}) &= \frac{\partial a_{\text{vp}}^{(k)}}{\partial \bar{\varepsilon}} : \dot{\bar{\varepsilon}} + \sum_l^{M_{\text{vp}}} \frac{\partial a_{\text{vp}}^{(k)}}{\partial \xi_{\text{vp}}^{(l)}} \times \dot{\xi}_{\text{vp}}^{(l)}, \text{ with } \dot{\xi}_{\text{vp}}^{(l)} = \frac{\partial \psi_{\text{vp}}^{\text{hom}}}{\partial a_{\text{vp}}^{(l)}} \\ \dot{a}_{\text{vp}}^{(k)} &= \frac{\partial a_{\text{vp}}^{(k)}}{\partial \bar{\varepsilon}} : \dot{\bar{\varepsilon}} + \frac{\partial \psi_{\text{vp}}^{\text{hom}}}{\partial \xi_{\text{vp}}^{(k)}}. \end{aligned} \quad (18)$$

$$\begin{aligned} \dot{a}_{\text{p},i}^{(k)}(\bar{\varepsilon}, \xi_{\text{p},i}) &= \frac{\partial a_{\text{p}}^{(k)}}{\partial \bar{\varepsilon}} : \dot{\bar{\varepsilon}} + \sum_l^{M_{\text{p},i}} \frac{\partial a_{\text{p}}^{(k)}}{\partial \xi_{\text{p},i}^{(l)}} \times \dot{\xi}_{\text{p},i}^{(l)}, \text{ with } \dot{\xi}_{\text{p},i}^{(l)} = \frac{\partial \psi_{\text{p}}^{\text{hom}}}{\partial a_{\text{p},i}^{(l)}} \\ \dot{a}_{\text{p},i}^{(k)} &= \frac{\partial \psi_{\text{p},i}^{\text{hom}}}{\partial \xi_{\text{p},i}^{(k)}}. \end{aligned}$$

At this stage and as it was done by Fritzen and Leuschner [9], one can be satisfied with these expressions to solve the reduced mechanical problem. Nevertheless, it is necessary at each time step to compute the local dissipation potential and then take its average over the whole volume. In other words, evaluating this expression is very time consuming. This model being used in the future within an industrial code of the fuel rod behaviour, it appeared necessary to use another approximation in order to obtain reasonable computational costs. This consists in approximating the homogenised dissipation potential with the tangent second-order linearization technique of Ponte Castaneda [7] around a so-called operating point, here the operating point retained is the average of the variables considered over a phase. This development is called TSO for Tangent Second Order. The TSO, carried out by [15], makes it possible to avoid the calculation of the homogenised dissipation potential at each time step. The local potential  $\psi$  is expanded to second-order and averaged over the phase:

$$\begin{aligned} \langle \psi_{\text{vp},s}^{\text{TSO}}(\mathcal{A}_{\text{vp},s}, \mathcal{A}_{\text{p},i}) \rangle^{(g)} &= \left[ \psi_{\text{vp},s}(\bar{\mathcal{A}}_{\text{vp},s}^{(g)}, \bar{\mathcal{A}}_{\text{p},i}^{(g)}) + \frac{\partial^2 \psi_{\text{vp},s}}{\partial \mathcal{A}_{\text{vp},s} \partial \mathcal{A}_{\text{p},i}} \times C^{(g)}(\mathcal{A}_{\text{vp},s}^{(g)}, \mathcal{A}_{\text{p},i}^{(g)}) \right. \\ &\quad \left. + \frac{1}{2} \frac{\partial^2 \psi_{\text{vp},s}}{\partial \mathcal{A}_{\text{vp},s}^2} \times C^{(g)}(\mathcal{A}_{\text{vp},s}^{(g)}) + \frac{1}{2} \frac{\partial^2 \psi_{\text{vp},s}}{\partial \mathcal{A}_{\text{p},i}^2} \times C^{(g)}(\mathcal{A}_{\text{p},i}^{(g)}) \right] - [\text{Dec}], \\ \langle \psi_{\text{p},i}^{\text{TSO}}(\mathcal{A}_{\text{vp},s}, \mathcal{A}_{\text{p},i}) \rangle^{(g)} &= \left[ \psi_{\text{p},i}(\bar{\mathcal{A}}_{\text{vp},s}^{(g)}, \bar{\mathcal{A}}_{\text{p},i}^{(g)}) + \frac{\partial^2 \psi_{\text{p},i}}{\partial \mathcal{A}_{\text{vp},s} \partial \mathcal{A}_{\text{p},i}} \times C^{(g)}(\mathcal{A}_{\text{vp},s}^{(g)}, \mathcal{A}_{\text{p},i}^{(g)}) \right. \\ &\quad \left. + \frac{1}{2} \frac{\partial^2 \psi_{\text{p},i}}{\partial \mathcal{A}_{\text{vp},s}^2} \times C^{(g)}(\mathcal{A}_{\text{vp},s}^{(g)}) + \frac{1}{2} \frac{\partial^2 \psi_{\text{p},i}}{\partial \mathcal{A}_{\text{p},i}^2} \times C^{(g)}(\mathcal{A}_{\text{p},i}^{(g)}) \right] - [\text{Dec}], \end{aligned} \quad (19)$$

$$\begin{aligned}
\langle \psi_{\text{vp},s}^{\text{TSO}}(\mathcal{A}_{\text{vp},s}, \mathcal{A}_{\text{p},i}) \rangle^{(g)} &= \psi_{\text{vp},s}(\bar{\mathcal{A}}_{\text{vp},s}^{(g)}, \bar{\mathcal{A}}_{\text{p},i}^{(g)}) + \frac{1}{2} \frac{\partial^2 \psi_{\text{vp},s}}{\partial \mathcal{A}_{\text{vp},s}^2} \times C^{(g)}(\mathcal{A}_{\text{vp},s}^{(g)}) - [\mathbf{Cpg}], \\
\langle \psi_{\text{p},i}^{\text{TSO}}(\mathcal{A}_{\text{vp},s}, \mathcal{A}_{\text{p},i}) \rangle^{(g)} &= \psi_{\text{p},i}(\bar{\mathcal{A}}_{\text{vp},s}^{(g)}, \bar{\mathcal{A}}_{\text{p},i}^{(g)}) + \frac{1}{2} \frac{\partial^2 \psi_{\text{p},i}}{\partial \mathcal{A}_{\text{vp},s}^2} \times C^{(g)}(\mathcal{A}_{\text{vp},s}^{(g)}) - [\mathbf{Cpg}],
\end{aligned} \tag{20}$$

with  $C^{(g)}(X, Y) = \langle (X - \bar{X}^{(g)}) (Y - \bar{Y}^{(g)}) \rangle^{(g)}$ ,  $C^{(g)}(X) = \langle (X - \bar{X}^{(g)})^2 \rangle^{(g)}$  and where  $\langle \cdot \rangle^{(g)} = \frac{1}{V^{(g)}} \times \int_V \cdot \chi^{(g)}(\mathbf{x}) d\mathbf{x}$ .

For the decomposed case, by combining (18) and (19) the evolution laws are expressed as:

$$\begin{aligned}
\dot{a}_{\text{vp}}^{(k)} &= \mathbf{a}^{(k)} : \dot{\bar{\boldsymbol{\varepsilon}}} \\
&+ \sum_g c^{(g)} \sum_s \left[ \frac{\partial \psi_{\text{vp},s}}{\partial \mathcal{A}_{\text{vp},s}} \left( \bar{\mathcal{A}}_{\text{vp},s}^{(g)}, \bar{\mathcal{A}}_{\text{p},i}^{(g)} \right) \times \frac{\partial \bar{\mathcal{A}}_{\text{vp},s}^{(g)}}{\partial \xi_{\text{vp}}^{(k)}} \right. \\
&+ \frac{1}{2} \frac{\partial^2 \psi_{\text{vp},s}}{\partial \mathcal{A}_{\text{vp},s}^2} \times \frac{\partial C^{(g)}}{\partial \xi_{\text{vp}}^{(k)}} \left( \mathcal{A}_{\text{vp},s}^{(g)} \right) + \frac{1}{2} \frac{\partial^3 \psi_{\text{vp},s}}{\partial \mathcal{A}_{\text{vp},s}^3} \times C^{(g)} \left( \mathcal{A}_{\text{vp},s}^{(g)} \right) \frac{\partial \bar{\mathcal{A}}_{\text{vp},s}^{(g)}}{\partial \xi_{\text{vp}}^{(k)}} \\
&+ \frac{1}{2} \frac{\partial^2 \psi_{\text{vp},s}}{\partial \mathcal{A}_{\text{p},i}^2} \times \frac{\partial C^{(g)}}{\partial \xi_{\text{vp}}^{(k)}} \left( \mathcal{A}_{\text{p},i}^{(g)} \right) + \frac{1}{2} \frac{\partial^3 \psi_{\text{vp},s}}{\partial \mathcal{A}_{\text{vp},s} \partial \mathcal{A}_{\text{p},i}^2} \times C^{(g)} \left( \mathcal{A}_{\text{p},i}^{(g)} \right) \frac{\partial \bar{\mathcal{A}}_{\text{vp},s}^{(g)}}{\partial \xi_{\text{vp}}^{(k)}} \\
&+ \left. \frac{\partial^2 \psi_{\text{vp},s}}{\partial \mathcal{A}_{\text{vp},s} \partial \mathcal{A}_{\text{p},i}} \times \frac{\partial C^{(g)}}{\partial \xi_{\text{vp}}^{(k)}} \left( \mathcal{A}_{\text{vp},s}^{(g)}, \mathcal{A}_{\text{p},i}^{(g)} \right) + \frac{\partial^3 \psi_{\text{vp},s}}{\partial \mathcal{A}_{\text{vp},s}^2 \partial \mathcal{A}_{\text{p},i}} \times C^{(g)} \left( \mathcal{A}_{\text{vp},s}^{(g)}, \mathcal{A}_{\text{p},i}^{(g)} \right) \frac{\partial \bar{\mathcal{A}}_{\text{vp},s}^{(g)}}{\partial \xi_{\text{vp}}^{(k)}} \right]
\end{aligned} \tag{21}$$

$$\begin{aligned}
\dot{a}_{\text{p},i}^{(k)} &= \sum_g c^{(g)} \sum_s \left[ \frac{\partial \psi_{\text{p},i}}{\partial \mathcal{A}_{\text{p},i}} \left( \bar{\mathcal{A}}_{\text{vp},s}^{(g)}, \bar{\mathcal{A}}_{\text{p},i}^{(g)} \right) \times \frac{\partial \bar{\mathcal{A}}_{\text{p},i}^{(g)}}{\partial \xi_{\text{p},i}^{(k)}} \right. \\
&+ \frac{1}{2} \frac{\partial^2 \psi_{\text{p},i}}{\partial \mathcal{A}_{\text{vp},s}^2} \times \frac{\partial C^{(g)}}{\partial \xi_{\text{p},i}^{(k)}} \left( \mathcal{A}_{\text{vp},s}^{(g)} \right) + \frac{1}{2} \frac{\partial^3 \psi_{\text{p},i}}{\partial \mathcal{A}_{\text{p},i} \partial \mathcal{A}_{\text{vp},s}^2} \times C^{(g)} \left( \mathcal{A}_{\text{vp},s}^{(g)} \right) \frac{\partial \bar{\mathcal{A}}_{\text{p},i}^{(g)}}{\partial \xi_{\text{p},i}^{(k)}} \\
&+ \frac{1}{2} \frac{\partial^2 \psi_{\text{p},i}}{\partial \mathcal{A}_{\text{p},i}^2} \times \frac{\partial C^{(g)}}{\partial \xi_{\text{p},i}^{(k)}} \left( \mathcal{A}_{\text{p},i}^{(g)} \right) + \frac{1}{2} \frac{\partial^3 \psi_{\text{p},i}}{\partial \mathcal{A}_{\text{p},i}^3} \times C^{(g)} \left( \mathcal{A}_{\text{p},i}^{(g)} \right) \frac{\partial \bar{\mathcal{A}}_{\text{p},i}^{(g)}}{\partial \xi_{\text{p},i}^{(k)}} \\
&+ \left. \frac{\partial^2 \psi_{\text{p},i}}{\partial \mathcal{A}_{\text{p},i} \partial \mathcal{A}_{\text{vp},s}} \times \frac{\partial C^{(g)}}{\partial \xi_{\text{p},i}^{(k)}} \left( \mathcal{A}_{\text{vp},s}^{(g)}, \mathcal{A}_{\text{p},i}^{(g)} \right) + \frac{\partial^3 \psi_{\text{p},i}}{\partial \mathcal{A}_{\text{vp},s} \partial \mathcal{A}_{\text{p},i}^2} \times C^{(g)} \left( \mathcal{A}_{\text{vp},s}^{(g)}, \mathcal{A}_{\text{p},i}^{(g)} \right) \frac{\partial \bar{\mathcal{A}}_{\text{p},i}^{(g)}}{\partial \xi_{\text{p},i}^{(k)}} \right]
\end{aligned}$$

For the constant per grain case, the evolutions laws can be deduced from (21) where the fluctuation per phase of the thermodynamic force associated with the strain hardening is equal to zero due to the decomposition made (13) and read as:  $C^{(g)}(\mathcal{A}_{\text{p},i}^{(g)}) = 0$ ,  $C^{(g)}(\mathcal{A}_{\text{vp},s}^{(g)}, \mathcal{A}_{\text{p},i}^{(g)}) = 0$ ,  $\frac{\partial C^{(g)}}{\partial \xi_{\text{p},i}^{(k)}}(\mathcal{A}_{\text{p},i}^{(g)}) = 0$ ,

$$\frac{\partial C^{(g)}}{\partial \xi_{\text{vp}}^{(k)}}(\mathcal{A}_{\text{vp},s}^{(g)}, \mathcal{A}_{\text{p},i}^{(g)}) = 0 \text{ and } \frac{\partial C^{(g)}}{\partial \xi_{\text{p},i}^{(k)}}(\mathcal{A}_{\text{vp},s}^{(g)}, \mathcal{A}_{\text{p},i}^{(g)}) = 0.$$

The terms composing the evolution laws (21) of reduced thermodynamics forces ( $\dot{\mathbf{a}}_{\text{vp}}^{(k)}$ ,  $\dot{a}_{\text{p},i}^{(k)}$ ) are functions of the macroscopic internal variables ( $\bar{\boldsymbol{\varepsilon}}$ ,  $\xi_{\text{vp}}$ ,  $\xi_{\text{p},i}$ ) weighted by precomputed quantities that need to be computed once. The coupled differential equations are integrated in time for a prescribed history

of the macroscopic strain ( $\bar{\epsilon}(t)$ ). This allows the determination of the resulting history of the reduced thermodynamics forces ( $a_{vp}^{(k)}(t)$ ,  $a_{p,i}^{(k)}(t)$ ). The reduced variables ( $\xi_{vp}(t)$ ,  $\xi_{p,i}(t)$ ) and the macroscopic stress  $\bar{\sigma}(t)$  are deduced using (16).

## 4 Results

A few cases of uniaxial compressive strain tests at imposed strain rate are used to illustrate the accuracy of the inverse calibration (comparison between full-field FFT and experimental results) and the accuracy of the reduced-order model (comparison between full-field FFT and NTFA-TSO model).

### 4.1 Effective response

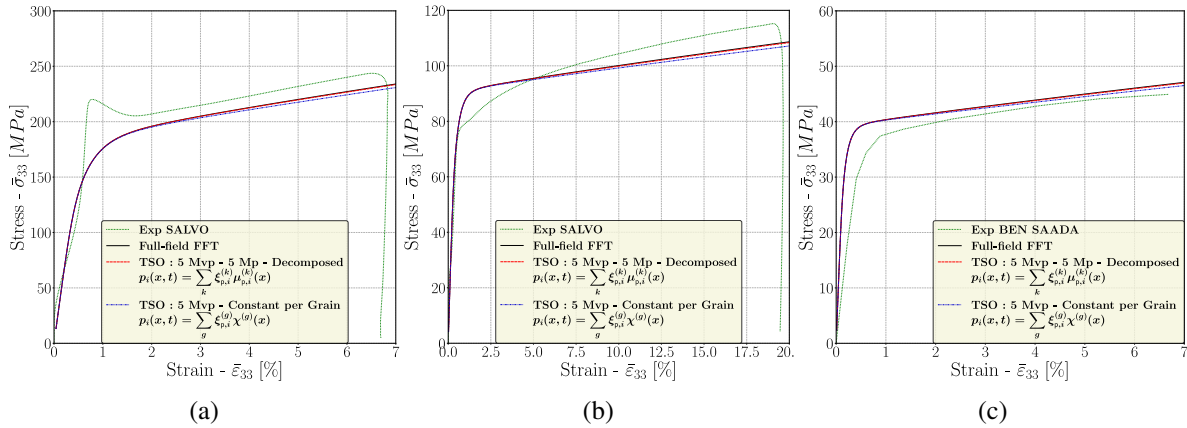


Figure 3: Comparison on uniaxial strain test of experimental results [13, 16] (green dashed line), full-field FFT simulation (black line) with evolution laws obtained with inverse calibration and the NTFA-TSO model (dashed line: red [Dec], blue [Cpg]) applied to the model at hand - Stress  $\bar{\sigma}_{33}$  as a function of strain  $\bar{\epsilon}_{33}$  for different loading conditions: **(a):**  $T = 1100 [^{\circ}C]$ ,  $\dot{\epsilon} = 10^{-1} [s]^{-1}$ , **(b):**  $T = 1700 [^{\circ}C]$ ,  $\dot{\epsilon} = 10^{-1} [s]^{-1}$ , **(c):**  $T = 1500 [^{\circ}C]$ ,  $\dot{\epsilon} = 10^{-6} [s]^{-1}$ .

The first two cases of study (**Figure 3:(a,b)** [13]) concern the available loading conditions which are closer to the loading conditions specific to the RIA. These two cases allow to check that the adopted formalism and the values of the parameters (8-12) intervening in (3) are able to account for the temperature dependence. The last case (**Figure 3:(c)** [16]) selected allows to test the strain rate dependence for a large spectrum of strain rates.

At the macroscopic level, as shown in **Figure 3**, there is a good agreement between the experimental tests [13, 16] on one hand and the FFT full-field simulations on the other. It indicates that the inverse calibration is relatively efficient especially for recovering the asymptotic behaviour. As can be seen in **Figure 3**, a very good agreement is found between NTFA-TSO and FFT full-field simulations for all three loading cases.

When the strain hardening variable is taken decomposed (13), the result is systematically better than when taken constant per grain. In particular, it seems that the strain hardening slope is better approximated with the first decomposition. The difference between the two decompositions, although increasing as the total strain increases, remains relatively small.

### 4.2 Local fields

A benefit of the NTFA method, already emphasized in [8, 11, 14, 15], is that the local fields can be easily reconstructed in a fairly straightforward manner from the knowledge of the reduced state variables and

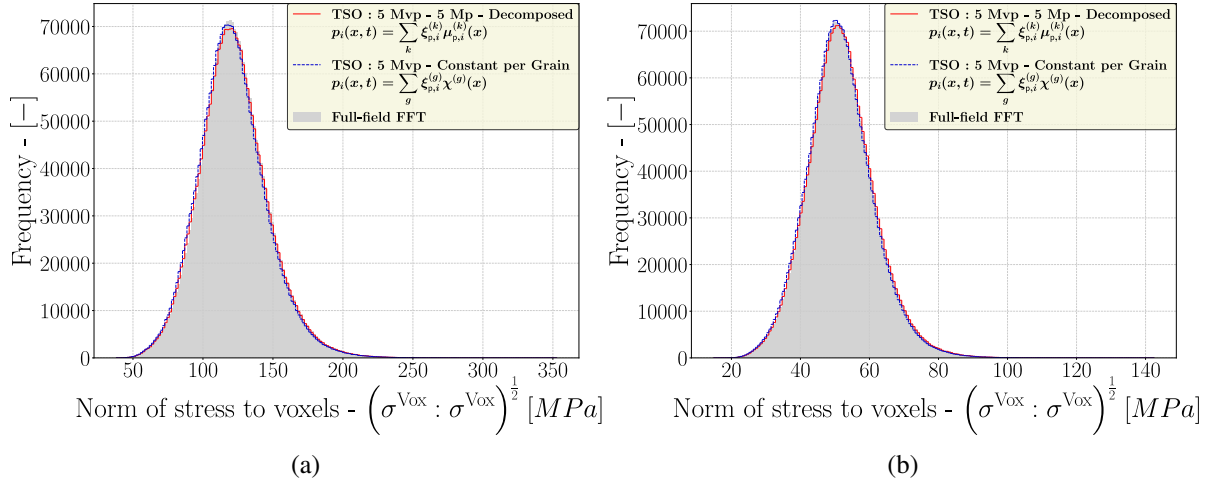


Figure 4: Comparison on uniaxial strain test of full-field FFT simulations (grey full) with evolution laws obtained with inverse calibration and the NTFA-TSO model (dashed line: red **[Dec]**, blue **[Cpg]**) - Probability distribution of a norm of the stress field for different loading conditions: **(a)**:  $\bar{\varepsilon}_{33} = 20$  [%],  $T = 1700$  [°C],  $\dot{\varepsilon} = 10^{-1}$  [s]<sup>-1</sup>, **(b)**:  $\bar{\varepsilon}_{33} = 7$  [%],  $T = 1500$  [°C],  $\dot{\varepsilon} = 10^{-6}$  [s]<sup>-1</sup>.

from pre-computed fields. This is the case of the local stress field which can be computed using (15). The probability distribution of a norm of the stress field  $\|\sigma\| = \sqrt{\sigma : \sigma}$  for different loading conditions as predicted by NTFA-TSO model match the distribution obtained with FFT full-field simulations (see **Figure 4**). The difference between the two decompositions, noticed at the macroscopic scale, is hardly perceptible at this scale.

## 5 Conclusion

An inverse calibration, through an iterative process, has been used to numerically determine a set of parameters that can account for the dependence of the viscoplastic behaviour law on the loading parameters. Once the parameters have been determined, a reduced order model (NTFA-TSO [15]) has been applied to the problem at hand by studying two different decompositions of the strain hardening variable. The accuracy of the inverse calibration and the reduced order model was studied for three different uniaxial compressive strain tests at given strain rate for different loading conditions. Macroscopically the FFT full-field simulations are in good agreement with the experimental results [13, 16]. Both macroscopically and locally, the reduced order model is in very good agreement with the FFT full-field simulations. The difference between the two decompositions, although increasing as the total strain increases, remains relatively small.

## References

- [1] R. Peierls, The size of a dislocation, Proceedings of the Physical Society, 52.1 (1940) pp. 34–37.
- [2] K. Levenberg, A method for the solution of certain non-linear problems in least squares, Quarterly of applied mathematics, 2.2 (1944) pp. 164–168.
- [3] D.W. Marquardt, An algorithm for least-squares estimation of nonlinear parameters, Journal of the society for Industrial and Applied Mathematics, 11.2 (1963) pp. 431–441.

- [4] J.F. Byron, The yield and flow of single crystals of uranium dioxide, *J. Nucl. Materials*, 28.1 (1968) pp. 110–114.
- [5] P.T. Sawbridge, E.C. Sykes, Dislocation glide in UO<sub>2</sub> single crystals at 1600 [K], *The Philosophical Magazine : A Journal of Theoretical Experimental and Applied Physics*, 24.187 (1971) pp. 33–53.
- [6] B.L. Mordike, Yield and flow of single crystals of uranium dioxide, *J. Nucl. Materials*, 60.2 (1976) pp. 223–226.
- [7] P. Ponte Castañeda, Exact second-order estimates for the effective mechanical properties of nonlinear composite materials, *J. Mech. Phys. Solids*, 44 (1996) pp. 827–862.
- [8] J.-C. Michel, P. Suquet, Nonuniform transformation field analysis, *Int. J. Solids Structures*, 40 (2003) pp. 6937–6955.
- [9] F. Fritzen, M. Leuschner, Reduced basis hybrid computational homogenization based on a mixed incremental formulation, *Comput. Methods Appl. Mech. Engrg.*, 260 (2013) pp. 143–154.
- [10] M. Knezevic, R.J. McCabe, C.N. Tomé, R.A. Lebensohn, S. Rong Chen, C.M. Cady, G.T. Gray III, B. Mihaila, Modeling mechanical response and texture evolution of  $\alpha$ -uranium as a function of strain rate and temperature using polycrystal plasticity, *International Journal of Plasticity*, 43.1 (2013) pp. 70–84.
- [11] R. Largenton, J.-C. Michel, P. Suquet, Extension of the nonuniform transformation field analysis to linear viscoelastic composites in the presence of aging and swelling, *Mechanics of Materials*, 73 (2014) pp. 76–100.
- [12] J. Soulacroix, Approche micromécanique du comportement du combustible dioxyde d'uranium, PhD Thesis École nationale supérieure d'arts et métiers-ENSAM, (2014) see p. 169.
- [13] M. Salvo, J. Sercombe, T. Helfer, P. Sornay, T. Desoyer, Experimental characterization and modelling of UO<sub>2</sub> grain boundary cracking at high temperatures and high strain rates, *J. Nucl. Materials*, 460 (2015) pp. 184–199.
- [14] J.-C. Michel, P. Suquet, A model-reduction approach in micromechanics of materials preserving the variational structure of constitutive relations, *J. Mech. Phys. Solids*, 90 (2016) pp. 254–285.
- [15] J.-C. Michel, P. Suquet, A model-reduction approach to the micromechanical analysis of polycrystalline materials, *Comput. Mech.*, 57.3 (2016) pp. 483–508.
- [16] M. Ben Saada, Étude du comportement visco-plastique du dioxyde d'uranium : quantification par analyse EBSD et ECCI des effets liés aux conditions de sollicitation et à la microstructure initiale, PhD Thesis Université de Lorraine, (2017).
- [17] L. Gelebart, J. Derouillat, AMITEX FFTP - Simulations FFT massivement parallèles en mécanique des matériaux hétérogènes, in *Proceedings of 13e colloque national en calcul des structures*, Giens, Var, France, (2017).
- [18] L. Portelette, J. Amodeo, R. Madec, J. Soulacroix, T. Helfer, B. Michel, Crystal viscoplastic modeling of UO<sub>2</sub> single crystal, *Journal of Nuclear Materials*, 510 (2018), pp 635–643